THE JOURNAL OF PHYSICAL CHEMISTRY C
A JOURNAL OF THE AMERICAN CHEMICAL SOCIETY

pubs.acs.org/JPCC
Article

Automatic Generation of Contrast Maps in Terms of van der Waals Material Properties in Bimodal AFM

Sergio Santos,*,# Lamiaa Elsherbiny,# Chia-Yun Lai, Khalid Askar,* Karim Gadelrab, and Matteo Chiesa

Cite This: J. Phys. Chem. C 2024, 128, 21154−21163

ABSTRACT: van der Waals (vdW) forces are of interest in colloid science, biophysics, cell biology, and the field of vdW heterostructures. We present a model and method to quantify vdW material properties of samples routinely in standard bimodal atomic force microscopy (AFM) without the need to establish mechanical contact with the samples. The method preserves the high resolution of bimodal AFM but enhances contrast by exploiting several transforms that lead to the production of contrast maps in the form of vdW material properties, i.e., Hamaker constant, adhesion, surface energy, peak forces, and surface energy hysteresis. We show that some of these maps provide information that is otherwise concealed in the raw channels.

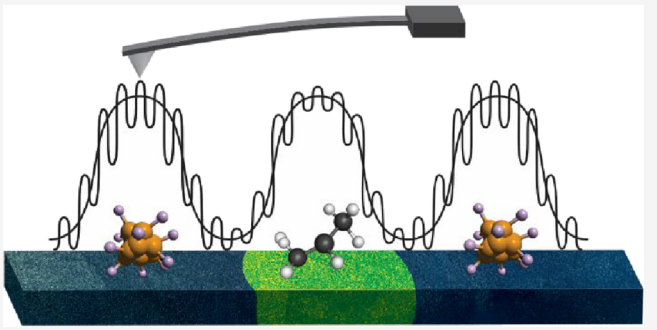

1. INTRODUCTION

The field of materials research and discovery advances by classifying materials into categories and by tabulating their properties.[1−6] In this work we deal with the characterization of long-range attractive forces in the nanoscale, generally termed van der Waals (vdW) forces. The phenomenon giving raise to vdW interactions between surfaces, molecules and nanoscale systems has gathered significant attention in recent years for several reasons. vdW forces allow for the construction, control and over stacking of materials[7] with nanoscale precision of arbitrary components at different twisting angles.[7−10] The current trend toward miniaturization led Zhang et al. to introduce the field of 2D electronics by stating that "the interface is the device".[7] Fields of research where vdW forces are exploited to develop advanced materials and systems include environmental[11] and colloid science,[12] biophysics and biomedical science,[13−16] optics and photonics,[8,17,18] spectrometry,[19] quantum computing,[20] medical devices,[21] imaging and therapy whereby vdW materials hold potential to overcome the drawbacks of individual materials,[21] and energy harvesting.[22,23] Arguably, the key to all these developments is the specific force profile and behavior of vdW interactions. The first attempts at measuring and quantifying vdW forces in atomic force microscopy (AFM) occurred quickly after its invention.[24−28] On the other hand, rapid, high resolution methods to routinely and robustly quantify vdW forces while imaging with an AFM are still being elucidated.[29,30] In particular, previous methods lack sufficient experimental implementations.[31] Furthermore, the vdW force might be complex[29,31] and advances in the field include material discovery in combination with Machine Learning (ML)[5,6,32,33] that aim at unraveling its particular behavior. The interested reader can refer to the introduction on the topic in a recent work by Gisbert and Garcia.[31] Finally, it is known that contrast in phase imaging (ϕ_1) in dynamic AFM is typically dependent on[34−36] the chosen free amplitudes A_0 (A_{01} and A_{02} for modes 1 and 2 respectively) and set-point amplitudes (A_1 and A_2). On the other hand, discriminating the origin of contrast in terms of intensive material properties related to dissipative or conservative phenomena, and even more, quantifying the origin of such contrast while imaging, remains challenging.

Here, we generalize bimodal AFM[37−42] (amplitude modulation AM-AM) to rapidly quantify vdW interactions with high resolution by exploiting a recently reported solution[43] to the governing integral equations in the multifrequency formalism. We experimentally explore two different systems in an air environment, i.e., calcite surfaces and single DNA molecules physisorbed on mica surfaces, and disentangle, quantify and interpret the dissipative and conservative contributions responsible for contrast in the raw images. The surface energy γ, peak force F_p and F_{AD} (force of adhesion) are derived from the parameters recovered from this formalism without the need of establishing mechanical contact. The implication is that the mechanical properties of soft single molecules like DNA,[44]

Received: September 6, 2024
Revised: November 16, 2024
Accepted: November 19, 2024
Published: November 26, 2024

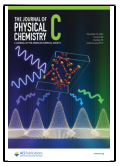

https://doi.org/10.1021/acs.jpcc.4c06040
J. Phys. Chem. C 2024, 128, 21154−21163

small proteins or antibodies,[45−47] can be probed and quantified with minimal invasiveness while maintaining high lateral resolution[48,49] and avoiding molecular damage or displacement.[31,47,50−54] Identifying and discriminating material properties of such systems while imaging and with minimal invasiveness holds potential to advance the study of biomolecular interactions with an AFM.[55−57] Other parameters worth mentioning that are recovered in the mode that we present in this work are the surface energy during tip approach (γ_a) and retraction (γ_r). We interpret the first as the conservative parameter controlling adhesion and we define the difference between the two as ε. This difference is the parameter controlling dissipation, i.e., adhesion hysteresis, in the long-range and can be identified with the long-range interfacial forces responsible for weak intermolecular bond formation and rupture.[58]

2. METHODS

Calcite ($CaCO_3$) is the most prevalent carbonate mineral and the most stable polymorph of calcium carbonate.[59,60] These calcite surfaces are known to give rise to two different domains that can be observed as compositional contrast in monomodal AFM images in the phase signal (ϕ_1).[60,61] The rhombohedral crystallographic structure of calcite ($CaCO_3$) leads to different cleavage planes.[62] This leads to the growth of surface islands, i.e., film growth. The islands are different chemical species, i.e., have different surface properties, depending on the crystallographic structure of the domain.[60] A main interpretation argues that the islands contain loosely bound water and hydrated calcium carbonate phases, i.e., a mineral composition typical of carbonate formations, that are stabilized by the calcite surface.[63] Its surface is otherwise atomically flat. Isolated DNA molecules physisorbed on mica surfaces have been model systems in soft matter imaging in AFM for decades[44,64] but new applications are ever emerging.[55,65−68] We have used these two samples as model systems in this work.

In bimodal AFM the cantilever is typically driven at or near the frequencies of the first and second flexural modes.[37] The relevant channels in our experiments are ϕ_1 (phase 1), ϕ_2 (phase 2), A_1 (amplitude 1) and A_2 (amplitude 2). Here, the first mode is used for feedback implying that the amplitude of the first mode A_1 should lead to none or minimal contrast and that any contrast should be uncorrelated to material properties. To avoid mechanical contact and repulsive interactions we employed the critical amplitude A_c method[69] whereby A_{01} is kept smaller than 1/3 A_c. A_c is the minimal value A_{01} for which transitions to the repulsive regime are not observed in amplitude and phase versus distance curves.[70] By keeping $A_{01} \ll A_c$ the likelihood of introducing repulsive forces in the interaction via mechanical contact is reduced. In our case, A_{01} = 4.8 nm (calcite) A_{01} = 3.7 nm (DNA on mica) and A_c was 21 and 18 nm, respectively.

The dynamics of the cantilever in bimodal AFM can be modeled as two coupled driven harmonic oscillators with the addition of the tip−sample force F_{ts}

$$m\ddot{z}_i = -k_i z_i - \frac{m\omega_{0i}}{Q_i}\dot{z}_i + \sum_{i=1}^{i=M} F_{0i}\cos\omega_i t + F_{ts}(z) \quad (1)$$

where m is the effective mass, k_i, Q_i and ω_{0i} are the spring constant, Quality factor and angular frequency of each mode i (i = 1 or 2 for modes 1 and 2) respectively. M stands for the number of modes. In our model M = 2 where F_{0i} and ω_i are the driving forces and frequencies of the modes, respectively. The tip−sample force is termed F_{ts} (z), and it is a function of cantilever instantaneous position z(t). The solutions to the above 2 equations can be simplified, by ignoring higher harmonics, to

$$z(t) = z_1(t) + z_2(t) + O(\varepsilon) \approx A_1\cos(\omega_1 t - \phi_1) + A_2\cos(\omega_2 t - \phi_2) \quad (2)$$

where A_1, A_2, ϕ_1 and ϕ_2 are the amplitudes and phases of modes 1 and 2 respectively. The above parameters are observables in bimodal AFM (the geometry of the system is shown schematically in Figure 1).

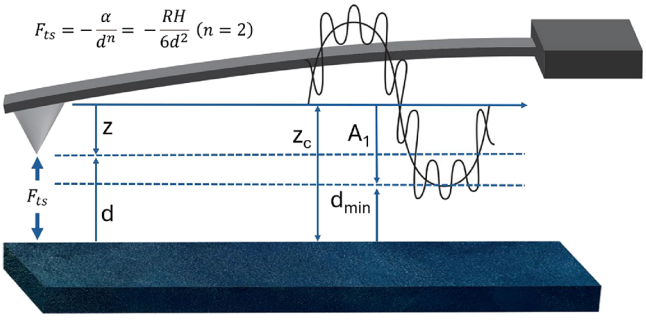

Figure 1. Schematic of an AFM cantilever from which geometrical expressions can be derived. All variables are defined in the main text. The force F_{ts} is generally expressed as an inverse square power law for vdW interactions.

3. RESULTS AND DISCUSSION

Figure 2 (top panels for calcite and bottom panels for DNA-mica) shows raw images obtained in bimodal AFM for the different observables (the height channel is not shown because it provides no information about the chemical composition of samples[30,71]). The first mode amplitude A_1 (panels 2(c) and 2(g) for the calcite and DNA samples respectively) leads to contrast at the edges of surface domains only (see also discussion on correlation with the help of Tables 1 and 2 below). This is consistent with a feedback based on A_1 and can be interpreted as the feedback error. The other channels are discussed below. Several points are worth mentioning about the other 3 channels, i.e., ϕ_1, ϕ_2 and A_2.

First, ϕ_1 provides contrast arising from mechanisms associated with dissipative forces.[72,73] In the long-range, this phenomenon can be understood as the formation and disruption of weak intermolecular bonds associated with the vdW forces at the molecular level.[58] Two domains are clearly observed on the calcite sample (Figure 2(a)) via the ϕ_1 channel but only the contour of the DNA molecule can be slightly observed (Figure 2(e)). Second, the second mode amplitudes A_2 and phases ϕ_2 are sensitive to conservative and dissipative forces.[74] For the samples above contrast is observed for these channels for the calcite sample between the two domains (Figures 2(b) and 2(d) respectively) and also between the mica surface and the DNA molecule (Figures 2(f) and 2(h) respectively). For the calcite sample, the implication is that the two domains differ in terms of both dissipative and conservative forces. For the DNA-mica system the implication is that conservative forces control image contrast in the second mode. Furthermore, the lack of contrast in ϕ_1 indicates a lack of difference in the magnitude of energy

https://doi.org/10.1021/acs.jpcc.4c06040
J. Phys. Chem. C 2024, 128, 21154−21163

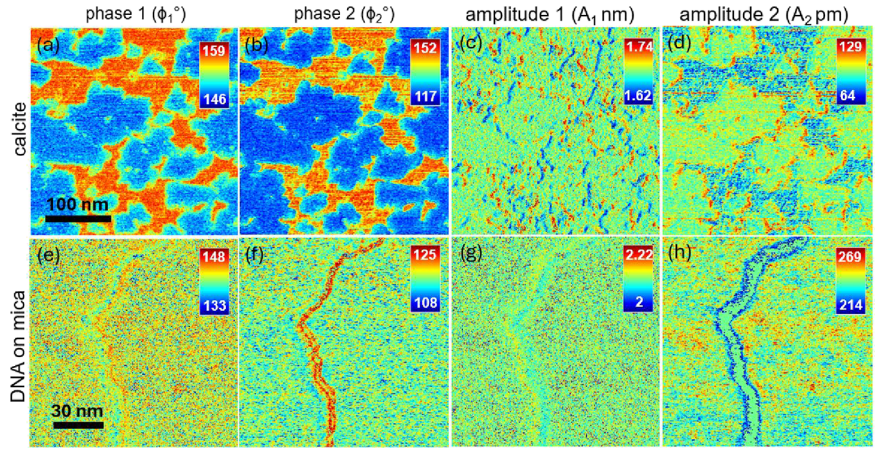

Figure 2. Images of the raw channels (ϕ_1, ϕ_2, A_1 and A_2) for the two samples (top panels for calcite and bottom panels for DNA-mica). Parameters in the experiments for the top panels (calcite): A_{01}= 4.8 nm, A_{02}= 150 pm, k_1= 2 N/m, k_2= 72 N/m, f_{01}= 71.287 kHz, f_{02}= 435.105 kHz, Q_1 = 104, Q_2 = 342, AmpInVolts1= 52 nm/V, AmpInVolts2= 15.0 nm/V, R = 10 nm (nominal value for OLYMPUS AC240TS cantilevers). Parameters in the experiments for the top bottom panels (DNA on mica): A_{01}= 3.7 nm, A_{02}= 320 pm, k_1= 2.06 N/m, k_2= 75 N/m, f_{01}= 79.212 kHz, f_{02}= 479.303 kHz, Q_1 = 104, Q_2 = 342, AmpInVolts1= 53 nm/V, AmpInVolts2= 15.3 nm/V, R = 10 nm (nominal value for OLYMPUS AC240TS cantilevers. The interpretation is given in the text.

Table 1. Correlation Coefficients (CC) for the Different Observables in Bimodal AFM (ϕ_1, Φ_2, A_1, A_2 and Height or Topography) against Each of the Recovered Parameters[a]

	ϕ_1		ϕ_2		A_1		A_2		height		eq
	calcite	mica DNA	calcite	mica DNA	calcite	mica DNA	calcite	mica DNA	calcite	mica DNA	
γ_a	−0.79	−0.03	−0.91	−0.85	0.18	0	0.7	0.65	−0.08	−0.07	17
H	−0.79	−0.03	−0.91	−0.85	0.18	0	0.7	0.65	−0.08	−0.07	19
F_{AD}	−0.79	0.03	−0.91	0.85	0.18	0	0.7	−0.65	−0.08	0.07	16
α	−0.79	−0.03	−0.91	−0.85	0.18	0	0.7	0.65	−0.08	−0.07	11
z_c	−0.8	−0.27	−0.91	−0.86	0.3	0.43	0.72	0.6	−0.09	−0.06	9
d_{min}	−0.83	−0.16	−0.94	−0.9	0.16	0.02	0.69	0.66	−0.09	−0.07	10
F_p	−0.91	−0.59	−0.98	−0.93	0.09	0.09	0.63	0.59	−0.11	−0.05	20
ε	−0.98	−0.87	−0.89	−0.39	−0.1	0.1	0.19	−0.4	−0.12	0.02	21
E_{T1}	1	−0.98	−0.93	−0.46	−0.03	0.09	0.33	0.03	−0.12	0.04	13
E_{T2}	−0.9	−0.3	−0.91	−0.38	−0.13	0.08	0.09	−0.72	−0.11	−0.05	14
E_{dis}	−0.99	−0.88	−0.94	−0.52	−0.05	0.1	0.29	0.31	−0.12	0.01	15

[a]The data corresponds to the data in Figs. 2-5. The interpretation is given in the text.

dissipation in the first mode between the substrate (mica) and the DNA molecule (to be discussed and corroborated later). Third, these two points can be employed to qualitative interpret the raw images in terms of material composition in monomodal (ϕ_1) and bimodal (A_1 and A_2) AFM. Furthermore, the two points also show that 1) monomodal AFM might fail to provide compositional contrast when the magnitude of dissipation is similar in two surface domains (see Figures 3 and 4 and discussion bellow) and that 2) enhanced contrast can be observed in the raw bimodal AFM images without the need of processing (compare Figure 2(e) with 1(g) and (h)). Next, we direct our attention to the recovery of material properties via the multifrequency formalism by modeling the tip−sample force F_{ts}.

The tip−sample instantaneous distance d (see Figure 1) can be written as

$$d = z_c + z \tag{3}$$

where z_c is the mean cantilever-surface separation.

The conservative force in the long-range can be reduced to the forces emerging from the fluctuations in the electric dipole moments of molecules or atoms,[75] i.e., the vdW forces. For systems like an AFM modeled as a sphere of radius R (R∼ 10 nm) and a flat surface, i.e., the sample, the dipoles become correlated as the respective systems come closer together at distances of approximately 1 nm and the correlation manifests as measurable forces. These forces are always present and attractive and can be written as a power law[28]

$$F_{ts} = -\frac{\alpha}{d^2},\ \mathrm{d} > \mathrm{a}_0 \tag{4}$$

where a_0 is an intermolecular distance, or cutoff distance,[75] that represents an effective yet nonrigorously well-defined, minimum distance between the tip and the surface. For systems composed of many atoms or molecules $a_0 \approx 0.165$ nm.[75] The parameter α in (4) defines the magnitude of the force and its units are N·m^2. From the Hamaker approach[76] and a tip−surface interaction (5) can be rewritten as

$$F_{ts} = -\frac{RH}{6d^2},\ \mathrm{d} > \mathrm{a0} \tag{5}$$

where H is the Hamaker constant. This parameter is defined in terms of intensive properties about the interacting materials such as the atomic density, the strength of the atom−atom

https://doi.org/10.1021/acs.jpcc.4c06040
J. Phys. Chem. C 2024, 128, 21154−21163

Table 2. Correlation Coefficients (CC) for Some of the Recovered Parameters against Each Other[a]

		H	d_{min}	F_p	ε	E_{T1}	E_{T2}	E_{dis}
H	calcite	1	1	0.95	0.68	0.79	0.71	0.79
	mica/DNA	1	0.99	0.81	−0.12	0.04	−0.02	0.02
d_{min}	calcite	1	1	0.98	0.73	0.83	0.75	0.83
	mica/DNA	0.99	1	0.89	−0.01	0.17	0.01	0.13
F_p	calcite	0.95	0.98	1	0.84	0.91	0.83	0.9
	mica/DNA	0.81	0.89	1	0.37	0.59	0.11	0.5
ε	calcite	0.68	0.73	0.84	1	0.98	0.93	0.99
	mica/DNA	−0.12	−0.01	0.37	1	0.88	0.68	0.99
E_{T1}	calcite	0.79	0.83	0.91	0.98	1	0.9	1
	mica/DNA	0.04	0.17	0.59	0.88	1	0.3	0.9
E_{T2}	calcite	0.71	0.75	0.83	0.93	0.9	1	0.93
	mica/DNA	−0.02	0.01	0.11	0.68	0.3	1	0.69
E_{dis}	calcite	0.79	0.83	0.9	0.99	1	0.93	1
	mica/DNA	0.02	0.13	0.5	0.99	0.9	0.69	1
eq		19	10	20	21	13	14	15

[a]The data corresponds to the data in Figs. 2-5. The interpretation is given in the text.

vdW force (Hamaker approach) or dielectric properties (Lifshitz approach).[28] The values of Hamaker in air range[75] from 10 to 100 zepto Joules, i.e., approximately 0.1−1 eV in air and approximately an order of magnitude smaller in liquid mediums like water. The force function, here an inverse square law, and the dimensions of the tip (R) add to the geometrical characteristics of the force. We have recently shown[32] that it is possible to directly predict from experimental data (pixel per pixel in an image), and by exploiting machine learning (ML) algorithms, whether the power law in (4) and (5) is a good fit for the experimental data or whether other power laws might be a better fit. We have run the experimental raw data in Figure 2 through such algorithm and found that n = 2 was the best fit throughout (data not shown). In particular, for the calcite sample n= 2 was predicted for 65437 out of the 65536 pixels. For the DNA-mica the result was 65536 of 65536. Assuming that long-range dissipative interfacial forces are responsible for dissipation when $d > a_0$, the dissipative contribution can be written as[58]

$$F_{ts} = -\varepsilon\frac{\alpha}{d^2},\ d > a_0 \text{ and } \dot{d} > 0(\text{tipretraction}) \tag{6}$$

The dimensionless term ε can be understood as a normalized difference between α on approach (α_a) and retraction (α_r). The net force, conservative (4) plus dissipative (6) terms, can be compactly written as

$$F_{ts} = -\frac{\alpha}{(z_c+z)^2}(1+\varepsilon),\ d > a_0 \text{ and } \dot{d} > 0(\text{tip retraction}) \tag{7}$$

$$F_{ts} = -\frac{\alpha}{(z_c+z)^{22}},\ d > a_0 \text{ and } \dot{d} < 0(\text{tip approach}) \tag{8}$$

where the distance d has been written in terms of z_c and z (Figure 1) for the purpose of solving the integral equations as detailed elsewhere.[43] The unknowns z_c, α and d_{min} (minimum distance of approach as illustrated in Figure 1) in (7) and (8)

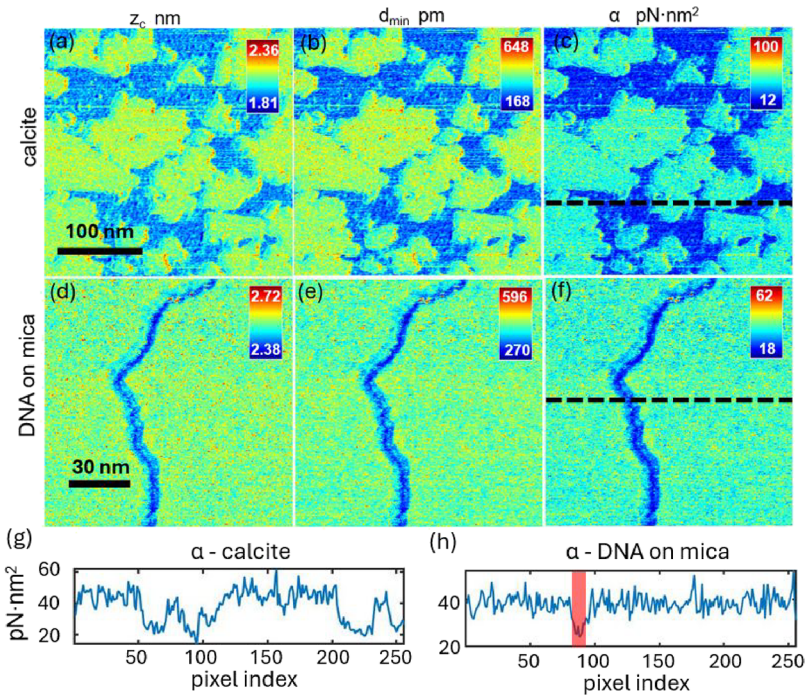

Figure 3. Reconstructed images for the parameters describing the dynamics of the system z_c ((a) and (d)) and d_{min} ((b) and (e)), and for the magnitude of the vdW force α ((c) and (f)) according to eqs 9 to (11) for the two samples (top panels for calcite and bottom panels for DNA-mica). Cross sections taken as indicated by the dashed line on (c) and (f) for the (g) calcite and (h) DNA on mica. The position where the DNA molecule should be found in the cross-section is highlighted in red in (h). The images are 256 by 256 pixels, and the DNA molecule is found at pixels ≈80−90 in the *x*-axis. Experimental parameters as in Figure 2.

https://doi.org/10.1021/acs.jpcc.4c06040
J. Phys. Chem. C 2024, 128, 21154−21163

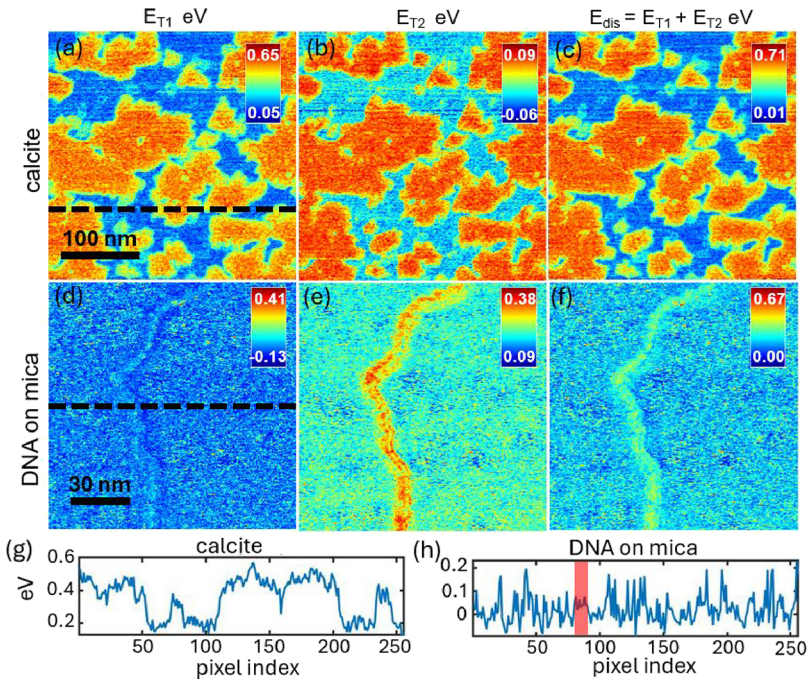

Figure 4. Reconstructed images for the magnitudes of energy transfer of modes 1 E_{T1} ((a) and (d)) and 2 E_{T2} ((b) and (e)) and for the total energy dissipated into the sample E_{dis} ((c) and (f)) according to eqs 13 to (15) for the two samples (top panels for calcite and bottom panels for DNA-mica). Cross sections taken as indicated by the dashed line on (a) and (d) for the (g) calcite and (h) DNA on mica. The position where the DNA molecule should be found in the cross-section is highlighted in red in (h). The images are 256 by 256 pixels, and the DNA molecule is found at pixels ≈80−90 in the *x*-axis. Experimental parameters as in Figure 2.

can be obtained from experimental observables by considering conservative forces alone[43]

$$z_c = A_1\left(\frac{1 + b/2}{1 - b}\right)^{1/2} \text{ where } b = \left[\frac{A_2}{A_1}\right]^2 \frac{F_{01}A_1\cos\phi_1}{F_{02}A_2\cos\phi_2} \tag{9}$$

$$d_{\min} \approx z_c - A_1 \tag{10}$$

$$\alpha = \frac{1}{2}F_{01}A_1^2\cos\phi_i\left[\left(\frac{z_C}{A_1}\right)^2 - 1\right]^{3/2} \tag{11}$$

The driving forces F_{0i} can be computed from observables

$$F_{0i} = \frac{k_i A_{0i}}{Q_i} \text{where } \omega i \approx \omega_{0i} \tag{12}$$

The transformations from the raw data in Figure 2 to z_c, $d_{\min}$ and α are shown in Figure 3 for the calcite (top panels) and the DNA-mica (bottom panels) systems. The two domains of calcite provide contrast in z_c (Figure 3(a)) implying that contrast in apparent height is compromised. This is because, for an ideal system relying on an amplitude feedback A_1 the separation z_c should be constant. The interpretation is that the "blue" domains will appear lower in height than they really are in relation to the "yellow" domains in the image. This is corroborated by observing that the average values of both z_c and $d_{\min}$ (Figure 3(b)) are lower in those domains. The difference in mean values is approximately 150 pm implying that the lower domains will appear 150 pm lower in the topography images than they really are due to this phenomenon (topography not shown). This loss of apparent height, and lower values of z_c and $d_{\min}$ for the "blue" domains, can be partly explained by the lower magnitude of the vdW forces in those domains as shown in Figure 3(c) with the use of α. The transform from α to R is direct since α=RH/6 (R≈ 10 nm). From the above expected values for H, the expected range of values for α for these systems is ≈20- 170 pN·nm^2. These expected values for α are in close agreement with the recovered data in Figures 3(c) and (f) for the calcite and DNA-mica systems, respectively. Cross sections for the *x*-axis for the (g) calcite and (h) DNA on mica are given for α in Figure 3 as indicated by the dashed lines in (c) and (f). The position where the DNA molecule should be found in the cross-section is highlighted in red in (h). The corresponding mean values for H for both samples are 0.15 and 0.14 eV for the calcite and DNA-mica systems, respectively.

The magnitude of the energy dissipated in the tip−sample interaction can be obtained without invoking any model. This comes with the advantage that model-free maps of energy dissipation can be produced. When there are two external drives, however, as in bimodal AFM, the energy delivered by the drive might be dissipated into the medium or the sample but also transferred between modes.[49,77,78] The expressions derived here ((13) and (14)) for each individual mode cannot differentiate between energy transfer to a mode or dissipated to the sample. For this reason, we speak of energy transfer E_T of modes one E_{T1} and two E_{T2}

$$E_{T1} \approx \pi F_{01}A_1\left[\sin\phi_1 - \frac{A_1}{A_{01}}\right] \tag{13}$$

$$E_{T2} \approx 6\pi F_{02}A_2\left[\sin\phi_2 - \frac{A_2}{A_{02}}\right] \tag{14}$$

The energy dissipated to the sample is the addition of the above two terms

https://doi.org/10.1021/acs.jpcc.4c06040
J. Phys. Chem. C 2024, 128, 21154−21163

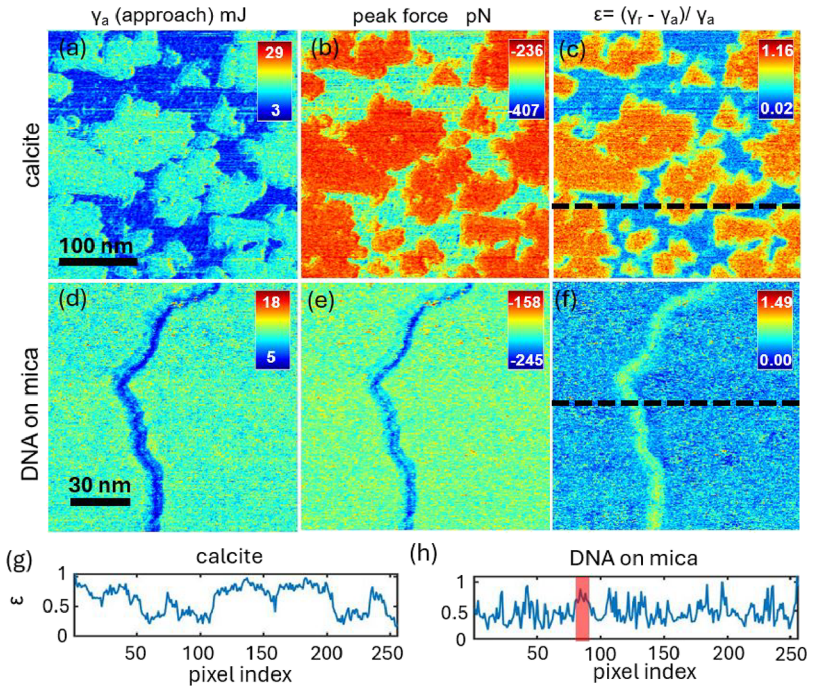

Figure 5. Reconstructed images for the surface energy during approach γ_a ((a) and (d)), the peak force ((b) and (e)) and the normalized difference in surface energy ε ((c) and (f)) according to eqs 17, (20and (21) respectively for the two samples (top panels for calcite and bottom panels for DNA-mica). Cross sections taken as indicated by the dashed line on (c) and (f) for the (g) calcite and (h) DNA on mica. The position where the DNA molecule should be found in the cross-section is highlighted in red in (h). The images are 256 by 256 pixels, and the DNA molecule is found at pixels ≈80−90 in the *x*-axis. Experimental parameters as in Figure 2.

$$E_{dis} \approx E_{T1} + E_{T2} \tag{15}$$

The implication is that E_{T1} and/or E_{T2} might be negative or positive, but E_{dis} must always be positive since the sample cannot deliver energy to the drives. The experimental results for the calcite and DNA-mica systems for (13) to (15) are shown in Figure 4. Cross sections for the *x*-axis for the (g) calcite and (h) DNA on mica are given for E_{T1} in Figure 4 as indicated by the dashed lines in (a) and (d). The position where the DNA molecule should be found in the cross-section is highlighted in red in (h). Arguably, only the outline of the DNA molecule can be distinguished in the E_{T1} channel (Figures (d) and (g)) while the domains on the calcite sample are easily distinguished by inspection (Figures (a) and (h)). We further reduced the contrast to a 0.2 eV range for Figures (d) to (f) for the DNA on mica sample to visually inspect the contrast of each channel (see supplementary Figure S4). Arguably, even at that range the DNA molecule can be better distinguished via the E_{T2} (Figure S4e) channel, less so via the E_{dis} (Figure S 4f) channel and even less so via the E_{T1} (Figure S 4d) channel. The results in Figure 4 seem to agree with our interpretation above since contrast is observed in both domains for the calcite sample in all channels but mostly in the signals that incorporate significant information about the second mode (E_{T2} and E_{dis}) for the DNA-mica system (see discussions on correlation between ϕ_1 and conservative parameters in Table 1. Bimodal imaging in the attractive regime thus provides information about material composition where monomodal AFM might fail. Furthermore, phase imaging in monomodal AFM with gentle interactions might not even provide enough contrast to clearly resolve the molecule (Figure 4(d)).

Next we discuss a further transformation of the parameters in (9) to (11) and the combination with (13) to (15). First, the standard vdW model in (4) and (5) can be made to provide information[75] about surface energy γ (half the interaction energy at contact) with the use of the following identities

$$F_{AD} = -4\pi R\gamma_a \text{ and } F_{AD} = -\frac{\alpha}{a_0^2} = -\frac{RH}{6a_0^2} \tag{16}$$

where γ_a stands for the adhesion force F_{AD} (minima in force) during tip approach and can be identified with γ in its standard definition. The reader should note that this interpretation assumes that adhesion is mainly due to vdW forces. While this is a simplification, the identity is in relative agreement with experiment in many cases.[75] Importantly, and in all cases, the identity gives the "true" adhesion due to vdW. Then

$$\gamma_a = \frac{\alpha}{4\pi R a_0^2}, \gamma \text{ on approach} \tag{17}$$

$$\gamma_r = \gamma_a(1 + \varepsilon), \gamma \text{ on retraction} \tag{18}$$

$$H \equiv \frac{6\alpha}{R} \tag{19}$$

It follows from (16) to (19) that α, γ (γ_a), H and F_{AD} are proportional according to this model. This means that quantification of all parameters in (16) to (19) is possible from (9) to (11) alone but no further contrast can be obtained from these transforms (see Tables 1 and 2 bellow and discussion). For this reason, we only show contrast in α (Figure 3) and γ_a (Figure 5).

Second, the peak force can be derived from (4) or (5) since all the parameters are known from (9) to (11). Then,

https://doi.org/10.1021/acs.jpcc.4c06040
J. Phys. Chem. C 2024, 128, 21154−21163

$$F_p(peak\ force) = -\frac{\alpha}{d_{min}^2} \equiv -\frac{RH}{6d_{min}^2},\ d > a0 \tag{20}$$

Finally, by combining the dissipative term ε in (6) and (7) where ($\varepsilon = 0$ on tip approach and $\varepsilon \equiv (\gamma_r\text{-}\gamma_a)/\gamma_a$ on tip retraction).

$$F_{ts} = -\frac{\alpha}{d^2}\left(1 + \frac{\gamma_r - \gamma_a}{\gamma_a}\right), d > a_0 \text{ and } \dot{d} > 0 (\text{tip retraction}) \tag{21}$$

It follows from (21) that ε can also be understood as the normalized difference in surface energy during tip approach (γ_a) and retraction (γ_r). The expression in (21) indicates that the magnitude in energy dissipation originates from the hysteresis in surface energy due to interfacial forces and it is equivalent to a difference in α on tip approach and retraction. The experimental results for γ_a in (17), the peak force F_p in (20) and $\varepsilon = (\gamma_r\text{-}\gamma_a)/\gamma_a$ in (21) are shown in Figure 5. Cross sections for the x-axis for the (g) calcite and (h) DNA on mica are given for ε in Figure 5 as indicated by the dashed lines in (c) and (f). The position where the DNA molecule should be found in the cross-section is highlighted in red in (h).

Several points are worth mentioning. First, the results corroborate the idea that phase imaging ϕ_1 with the first mode cannot resolve differences that originate only from forces related to intensive conservative parameters such as γ_a (or equivalently to α, H or F_{AD} since these are proportional). Second, peak forces F_p are larger (in absolute terms since the force is negative) where the conservative force is smaller, that is where α or γ_a are smaller (Figures 3 and 5). In particular, the peak force gets very close to a_0 even with the use of relatively small first mode free amplitudes (A_{01}< 5 nm). The implication is that for attractive mode imaging and to avoid establishing mechanical contact with isolated soft molecules such as DNA, the free amplitudes should remain small, i.e., A_{01} < 5 nm. This is consistent with our latest theoretical findings.[43] Third, while the expressions to quantify energy transfer between modes and the sample (13) to (15) provide information about the magnitude of energy dissipated, they fail to quantitatively provide information about the properties of the material responsible for dissipation. Compare the raw images for ϕ_1 in Figure 2 (a) and (d) for the calcite and DNA-mica systems with the results in terms of energy transfer by mode 1 (E_{T1}) in Figures 4 (a) and (d) (and γ_a in Figures 5 (a) and (d) in relation to the fist point above). Furthermore, contrast might be missing when plotting the magnitude of energy dissipation (see Figure 4(d)) but present (see Figure 5(f)) when plotting the actual material property responsible for dissipation (ε or equivalently $(\gamma_r\text{-}\gamma_a)/\gamma_a$). This is because while ε is a property of the material related to dissipation, the energy dissipated per cycle is also related to conservative parameters, i.e., γ_a or α, that the ϕ_1 channel alone might not fully resolve. This implies that recovering both the conservative parameter γ_a in Figure 5 (or α in (4) as shown in Figure 3 since they are proportional) and the transformation in (21) that leads to recovering ε (or equivalently γ_r) are required to better characterize dissipative material properties in the long-range where vdW forces dominate the interaction. This is the situation for the DNA-mica system where low contrast is observed in ϕ_1 (Figure 2(e)) and E_{T1} (Figure 4(d)) but good contrast is obtained in terms of γ_a (Figure 5(d)) and ε (Figure 5(f)). For the calcite sample contrast is observed between the two domains throughout. This is because both the magnitude of energy in terms of E_{T1} (Figure 4(a)) and the material properties corresponding to conservative interactions, i.e., γ_a in Figure 5(a) or α in Figure 3(c)), are larger on the same domains.

The above interpretation can be further corroborated and better informed by computing the correlation coefficients (CC) between the different parameters. Table 1 shows the correlation coefficients for both samples in terms of the observables or raw channels in Figure 2 and several recovered parameters. The discussion centers on ϕ_1, ϕ_2 and A_2 since, as discussed in the introduction, the channels A_1 and height or topography do not provide direct information about material composition. This agrees with the CC values for these channels as provide in Table 1 where ||CC|| < 0.2 throughout. The properties reported in Table 1 include those related to conservative forces, i.e., γ_a (surface energy of approach or simply surface energy), H (Hamaker constant), F_{AD} (adhesion force), the three parameters recovered from the multifrequency formalism, i.e., α, z_c (mean cantilever-surface separation), and d_{min} (minimum distance of approach), F_p (peak force) and the components related to transfer of energy between modes, i.e., E_{T1} and E_{T2}, and the dissipative components ε and E_{dis}. The equations employed for each parameter are also provided in the table.

The data shows that the two calcite domains should be observed as contrast from phase 1 (ϕ_1), phase 2 (ϕ_2) and Amplitude 2 (A_2) since there is some correlation for all variables, i.e., ||CC|| > 0.5. On the other hand, for the DNA-mica system, significant correlation is observed only for the signals of mode 2, i.e., phase 2 (ϕ_2) and Amplitude 2 (A_2). This is consistent with the data shown in Figure 2 (top panels for calcite and bottom panels for DNA-mica) and the discussion above. Furthermore, γ_a, H, F_{AD} and α have the same correlation, i.e., contrast in terms of images, to all the raw channels. This is also consistent with the fact that these parameters are proportional to each other. The data in Table 1 also shows that the CC values for ε and the raw channels are significant for both samples. This is also in agreement with the discussion above. Finally, CC values are also reported for most of the recovered parameters against each other in Table 2. The most important detail in Table 2, and in relation to the discussion above, is that the conservative parameters (H in Table 1 but the values are the same for γ_a, F_{AD} and α) have low correlation to the magnitudes in energy as computed via E_{T1}, E_{T2} and E_{dis} for the DNA-mica system. For the same system, high correlation is observed for the material property related to dissipation ε and the E_{T1}, E_{T2} and E_{dis} channels. For the calcite sample, the CC values are significant between all parameters. In agreement with the interpretation so far, this is because the domains where less magnitude of energy is computed in terms of E_{T1}, E_{T2} and E_{dis} coincide with the domains with lower values of properties related to conservative interactions, i.e., α or H, are found.

4. CONCLUSIONS

As a final note, it is worth mentioning that nonspecific "vdW bonds" or contacts are typically formed at distances close to a_0 (~ 0.2 nm).[75,79] These are distances similar to the minimum distance of approach d_{min} (Figures 3(b) and (e)). The typical bond energy associated with these "vdW bonds" is ~ kT (approximately 0.02 eV). Since the energy dissipated per cycle (E_{dis}) for the calcite sample goes from 0.01 to 0.71 eV (Figure 4(c)), the equivalent number of "vdW bonds" leading to

https://doi.org/10.1021/acs.jpcc.4c06040
J. Phys. Chem. C 2024, 128, 21154−21163

dissipation is 1 to 27. For the DNA-mica system E_{dis} = 0−0.67 eV (Figure 4(f)) or approximately 0 to 26 vdW bonds. The peak force can also be related to the number of vdW interactions originating from conservative interactions. A typical vdW interaction leads to ≈40 pN. For the calcite sample the peak force goes from −236 to −407 pN. The equivalent in terms of full vdW interactions is 6−10. For the DNA-mica system the force goes from −158 to −245 pN, i.e., 4 to 6 vdW interactions. In summary, we have presented a comprehensive formalism to probe, quantify and interpret conservative and dissipative vdW forces in bimodal AFM. The formalism can be applied without compromising resolution or speed in multifrequency AFM. While more complex force models might be required to understand certain vdW systems and behavior, the present methods can be routinely applied with standard AFM equipment.

■ ASSOCIATED CONTENT

Supporting Information

The Supporting Information is available free of charge at https://pubs.acs.org/doi/10.1021/acs.jpcc.4c06040.

Energy transfer of mode 1 E_{T1} (Figure S1); energy transfer of mode 2 E_{T2} (Figure S2); energy dissipation E_{dis} (Table S3); and reconstructed images for the magnitudes of energy transfer of modes 1 E_{T1} and 2 E_{T2} and for the total energy dissipated into the sample E_{dis} (Figure S4) (PDF)

■ AUTHOR INFORMATION

Corresponding Authors

Sergio Santos − *Department of Physics and Technology, UiT-the Arctic University of Norway, Tromsø 9037, Norway;* orcid.org/0000-0003-0448-1668; Email: ssantos78h@gmail.com

Khalid Askar − *Laboratory for Energy and NanoScience (LENS), Khalifa University of Science and Technology, 127788 Abu Dhabi, United Arab Emirates;* Email: khalid.askar@ku.ac.ae

Authors

Lamiaa Elsherbiny − *Laboratory for Energy and NanoScience (LENS), Khalifa University of Science and Technology, 127788 Abu Dhabi, United Arab Emirates*

Chia-Yun Lai − *Laboratory for Energy and NanoScience (LENS), Khalifa University of Science and Technology, 127788 Abu Dhabi, United Arab Emirates*

Karim Gadelrab − *Department of Materials Science and Engineering, Massachusetts Institute of Technology, Cambridge, Massachusetts 02139, United States;* orcid.org/0000-0002-6000-3364

Matteo Chiesa − *Department of Physics and Technology, UiT-the Arctic University of Norway, Tromsø 9037, Norway; Laboratory for Energy and NanoScience (LENS), Khalifa University of Science and Technology, 127788 Abu Dhabi, United Arab Emirates;* orcid.org/0000-0001-8170-5288

Complete contact information is available at: https://pubs.acs.org/10.1021/acs.jpcc.4c06040

Author Contributions

#Equally contributing authors.

Notes

The authors declare no competing financial interest.

■ ACKNOWLEDGMENTS

We acknowledge Maritsa Kissamitaki for the artwork. This research is supported by ASPIRE, the technology program management pillar of Abu Dhabi's Advanced Technology Research Council (ATRC), via the ASPIRE VRI (Virtual Research Institute) Award No. VRI20-07.

■ REFERENCES

(1) Callister, W. D.; Rethwisch, D. G. *Fundamentals of Materials science and engineering: An Integrated Approach*. John Wiley & Sons: 2020.

(2) Choudhary, K.; DeCost, B.; Chen, C.; Jain, A.; Tavazza, F.; Cohn, R.; Park, C. W.; Choudhary, A.; Agrawal, A.; Billinge, S. J. L.; et al. Recent advances and applications of deep learning methods in materials science. *npj Comput. Mater.* **2022**, *8* (1), 59.

(3) *Materials science*. Britannica: https://www.britannica.com/technology/materials-science, 2024.

(4) Cross, J. O.; Opila, R. L.; Boyd, I. W.; Kaufmann, E. N. Materials characterization and the evolution of materials. *MRS Bull.* **2015**, *40* (12), 1019−1034.

(5) Kusne, A. G.; Yu, H.; Wu, C.; Zhang, H.; Hattrick-Simpers, J.; DeCost, B.; Sarker, S.; Oses, C.; Toher, C.; Curtarolo, S.; et al. On-the-fly closed-loop materials discovery via Bayesian active learning. *Nat. Commun.* **2020**, *11* (1), 5966.

(6) López, C. Artificial Intelligence and Advanced Materials. *Adv. Mater.* **2023**, *35* (23), No. 2208683.

(7) Zhang, X.; Zhang, Y.; Yu, H.; Zhao, H.; Cao, Z.; Zhang, Z.; Zhang, Y. Van der Waals-Interface-Dominated All-2D Electronics. *Adv. Mater.* **2023**, *35* (50), No. 2207966.

(8) Guo, X.; Lyu, W.; Chen, T.; Luo, Y.; Wu, C.; Yang, B.; Sun, Z.; García de Abajo, F. J.; Yang, X.; Dai, Q. Polaritons in Van der Waals Heterostructures. *Adv. Mater.* **2023**, *35* (17), No. 2201856.

(9) Hou, H.-L.; Anichini, C.; Samorì, P.; Criado, A.; Prato, M. 2D Van der Waals Heterostructures for Chemical Sensing. *Adv. Funct. Mater.* **2022**, *32* (49), No. 2207065.

(10) Oh, S.-H.; Altug, H.; Jin, X.; Low, T.; Koester, S. J.; Ivanov, A. P.; Edel, J. B.; Avouris, P.; Strano, M. S. Nanophotonic biosensors harnessing van der Waals materials. *Nat. Commun.* **2021**, *12* (1), 3824.

(11) Xu, C.-y.; Zhou, T.-t.; Wang, C.-l.; Liu, H.-y.; Zhang, C.-t.; Hu, F.-n.; Zhao, S.-w.; Geng, Z.-c. Aggregation of polydisperse soil colloidal particles: Dependence of Hamaker constant on particle size. *Geoderma* **2020**, *359*, No. 113999.

(12) Wang, H.; Evans, D.; Voelcker, N. H.; Griesser, H. J.; Meagher, L. Modulation of substrate van der Waals forces using varying thicknesses of polymer overlayers. *J. Colloid Interface Sci.* **2020**, *580*, 690−699.

(13) Jing, H.; Sinha, S.; Sachar, H. S.; Das, S. Interactions of gold and silica nanoparticles with plasma membranes get distinguished by the van der Waals forces: Implications for drug delivery, imaging, and theranostics. *Colloids Surf., B* **2019**, *177*, 433−439.

(14) Mohamed Zuki, F.; Edyvean, R. G. J.; Pourzolfaghar, H.; Kasim, N. Modeling of the Van Der Waals Forces during the Adhesion of Capsule-Shaped Bacteria to Flat Surfaces. *Biomimetics* **2021**, *6* (1), 5.

(15) Hajizadeh, K.; Mehdian, H.; Hajisharifi, K.; Robert, E. A van der Waals force-based adhesion study of stem cells exposed to cold atmospheric plasma jets. *Sci. Rep.* **2022**, *12* (1), 12069.

(16) Seo, S.; Kang, B.-S.; Lee, J.-J.; Ryu, H.-J.; Kim, S.; Kim, H.; Oh, S.; Shim, J.; Heo, K.; Oh, S.; et al. Artificial van der Waals hybrid synapse and its application to acoustic pattern recognition. *Nat. Commun.* **2020**, *11* (1), 3936.

(17) Meng, Y.; Zhong, H.; Xu, Z.; He, T.; Kim, J. S.; Han, S.; Kim, S.; Park, S.; Shen, Y.; Gong, M.; et al. Functionalizing nanophotonic structures with 2D van der Waals materials. *Nanoscale Horizons* **2023**, *8* (10), 1345−1365.

(18) He, J.; Wang, C.; Zhou, B.; Zhao, Y.; Tao, L.; Zhang, H. 2D van der Waals heterostructures: processing, optical properties and

applications in ultrafast photonics. *Materials Horizons* **2020**, *7* (11), 2903−2921.
(19) Uddin, M. G.; Das, S.; Shafi, A. M.; Wang, L.; Cui, X.; Nigmatulin, F.; Ahmed, F.; Liapis, A. C.; Cai, W.; Yang, Z.; et al. Broadband miniaturized spectrometers with a van der Waals tunnel diode. *Nat. Commun.* **2024**, *15* (1), 571.
(20) Antony, A.; Gustafsson, M. V.; Ribeill, G. J.; Ware, M.; Rajendran, A.; Govia, L. C. G.; Ohki, T. A.; Taniguchi, T.; Watanabe, K.; Hone, J.; et al. Miniaturizing Transmon Qubits Using van der Waals Materials. *Nano Lett.* **2021**, *21* (23), 10122−10126.
(21) Dai, J.; Chen, J.; Song, J.; Ji, Y.; Qiu, Y.; Hong, Z.; Song, H.; Yang, L.; Zhu, Y.; Li, L.; et al. Photodynamic therapy: When van der Waals heterojunction meets tumor. *Chemical Engineering Journal* **2021**, *421*, No. 129773.
(22) Widiapradja, L. J.; Hong, S.; Kim, K.-T.; Bae, H.; Im, S. Van der Waals crystal radio with Pt/MoSe2 Schottky diode and h-BN capacitor for RF energy harvesting. *Nano Energy* **2022**, *92*, No. 106771.
(23) Parmar, P. R.; Khengar, S. J.; Mehta, D.; Sonvane, Y.; Thakor, P. B. Solar energy harvesting by a PtS2/ZrS2 van der Waals heterostructure. *New J. Chem.* **2023**, *47* (32), 15162−15174.
(24) Hutter, J. L.; Bechhoefer, J. Measurement and manipulation of van der Waals forces in atomic-force microscopy. *Journal of Vacuum Science & Technology B: Microelectronics and Nanometer Structures Processing, Measurement, and Phenomena* **1994**, *12* (3), 2251−2253.
(25) Butt, H. J. Electrostatic interaction in atomic force microscopy. *Biophys. J.* **1991**, *60* (4), 777−85.
(26) Paulo, Á. S.; García, R. Tip-surface forces, amplitude, and energy dissipation in amplitude-modulation (tapping mode) force microscopy. *Phys. Rev. B* **2001**, *64* (19), No. 193411.
(27) Hartmann, U. van der Waals interactions between sharp probes and flat sample surfaces. *Physical review. B, Condensed matter* **1991**, *43* (3), 2404−2407.
(28) Israelachvili, J. N. *Intermolecular and Surface Forces*. Elsevier Academic Press: London, 2005.
(29) Santos, S.; Gadelrab, K.; Olukan, T.; Font, J.; Barcons, V.; Chiesa, M. Probing power laws in multifrequency AFM. *Appl. Phys. Lett.* **2023**, *122* (7), No. 071603.
(30) Lai, C.-Y.; Perri, S.; Santos, S.; Garcia, R.; Chiesa, M. Rapid quantitative chemical mapping of surfaces with sub-2 nm resolution. *Nanoscale* **2016**, *8* (18), 9688−9694.
(31) Gisbert, V. G.; Garcia, R. Fast and high-resolution mapping of van der Waals forces of 2D materials interfaces with bimodal AFM. *Nanoscale* **2023**, *15* (47), 19196−19202.
(32) Elsherbiny, L.; Santos, S.; Gadelrab, K.; Olukan, T.; Font, J.; Barcons, V.; Chiesa, M. Machine learning assisted multifrequency AFM: Force model prediction. *Appl. Phys. Lett.* **2023**, *123* (23), No. 231603.
(33) Cai, J.; Chu, X.; Xu, K.; Li, H.; Wei, J. Machine learning-driven new material discovery. *Nanoscale advances* **2020**, *2* (8), 3115−3130.
(34) Santos, S.; Barcons, V.; Font, J.; Thomson, N. H. Bi-stability of amplitude modulation AFM in air: deterministic and stochastic outcomes for imaging biomolecular systems. *Nanotechnology* **2010**, *21* (22), No. 225710.
(35) Legleiter, J. The effect of drive frequency and set point amplitude on tapping forces in atomic force microscopy: simulation and experiment. *Nanotechnology* **2009**, *20* (24), No. 245703.
(36) Damircheli, M.; Payam, A. F.; Garcia, R. Optimization of phase contrast in bimodal amplitude modulation AFM. *Beilstein Journal of Nanotechnology* **2015**, *6*, 1072−1081.
(37) Garcia, R.; Herruzo, E. T. The emergence of multifrequency force microscopy. *Nat. Nanotechnol.* **2012**, *7* (4), 217−226.
(38) Lozano, J. R.; Garcia, R. Theory of Multifrequency Atomic Force Microscopy. *Phys. Rev. Lett.* **2008**, *100*, 076102−076105.
(39) Yang, P.; Bi, Z.; Shang, Y.; Chen, K.; Liang, Y.; Li, X.; Shang, G. Bimodal AFM-Based Nanocharacterization of Cycling-Induced Topographic and Mechanical Evolutions of LiMn2O4 Cathode Films. *Langmuir* **2021**, *37* (21), 6406−6413.
(40) Lou, P.; Bi, Z.; Wang, X.; Shang, G. Visualization and Quantification of State of Charge-Dependent Young's Modulus of LiMn2O4 Nanosized Particles by Bimodal AFM. *Langmuir* **2024**, *40* (33), 17740−17746.
(41) Yamada, Y.; Ichii, T.; Utsunomiya, T.; Kimura, K.; Kobayashi, K.; Yamada, H.; Sugimura, H. Fundamental and higher eigenmodes of qPlus sensors with a long probe for vertical-lateral bimodal atomic force microscopy. *Nanoscale advances* **2023**, *5* (3), 840−850.
(42) Swierczewski, M.; Chenneviere, A.; Lee, L.-T.; Maroni, P.; Bürgi, T. Nanomechanical and structural study of Au38 nanocluster Langmuir-Blodgett films using bimodal atomic force microscopy and X-ray reflectivity. *J. Colloid Interface Sci.* **2023**, *630*, 28−36.
(43) Santos, S.; Gadelrab, K.; Elsherbiny, L.; Drexler, X.; Olukan, T.; Font, J.; Barcons, V.; Chiesa, M. Quantification of van der Waals forces in bimodal and trimodal AFM. *J. Chem. Phys.* **2023**, *158* (20), No. 204703.
(44) Lyubchenko, Y. L. Preparation of DNA and nucleoprotein samples for AFM imaging. *Micron* **2011**, *42* (2), 196−206.
(45) THOMSON, N. H. Imaging the substructure of antibodies with tapping-mode AFM in air: the importance of a water layer on mica. *J. Microsc.* **2005**, *217* (3), 193−199.
(46) Thomson, N. H. The substructure of immunoglobulin G resolved to 25 kDa using amplitude modulation AFM in air. *Ultramicroscopy* **2005**, *105* (1−4), 103−10.
(47) San Paulo, A.; Garcia, R. High-Resolution Imaging of Antibodies by Tapping-Mode Atomic Force Microscopy: Attractive and Repulsive Tip-Sample Interaction Regimes. *Biophys. J.* **2000**, *78*, 1599−1605.
(48) Kawai, S.; Glatzel, T.; Koch, S.; Such, B.; Baratoff, A.; Meyer, E. Systematic Achievement of Improved Atomic-Scale Contrast via Bimodal Dynamic Force Microscopy. *Phys. Rev. Lett.* **2009**, *103*, 220801−220804.
(49) Lai, C.-Y.; Santos, S.; Chiesa, M. Systematic Multidimensional Quantification of Nanoscale Systems From Bimodal Atomic Force Microscopy Data. *ACS Nano* **2016**, *10* (6), 6265−6272.
(50) Hansma, H. G.; Hoh, J. H. Biomolecular Imaging with the Atomic Force Microscope. *Annl. Rev. Biophys.* **1994**, *23* (Volume23, 1994), 115−140.
(51) Santos, S.; Thomson, N. H. Energy dissipation in a dynamic nanoscale contact. *Appl. Phys. Lett.* **2011**, *98*, 013101−013103.
(52) High-resolution atomic-force microscopy of DNA: the pitch of the double helix. *FEBS Lett.***1995**,*371* (3), 279−282.
(53) Magazzù, A.; Marcuello, C. Investigation of Soft Matter Nanomechanics by Atomic Force Microscopy and Optical Tweezers: A Comprehensive Review. *Nanomaterials* **2023**, *13* (6), 963.
(54) Forchheimer, D.; Platz, D.; Tholén, E. A.; Haviland, D. B. Model-based extraction of material properties in multifrequency atomic force microscopy. *Phys. Rev. B* **2012**, *85* (19), No. 195449.
(55) Amyot, R.; Nakamoto, K.; Kodera, N.; Flechsig, H. Predicting the placement of biomolecular structures on AFM substrates based on electrostatic interactions. *Front. Mol. Biosci.* **2023**, *10*, No. 1264161.
(56) Lostao, A.; Lim, K.; Pallarés, M. C.; Ptak, A.; Marcuello, C. Recent advances in sensing the inter-biomolecular interactions at the nanoscale − A comprehensive review of AFM-based force spectroscopy. *Int. J. Biol. Macromol.* **2023**, *238*, No. 124089.
(57) Miryala, S. K.; Anbarasu, A.; Ramaiah, S. Discerning molecular interactions: A comprehensive review on biomolecular interaction databases and network analysis tools. *Gene* **2018**, *642*, 84−94.
(58) Garcia, R.; Gómez, C. J.; Martinez, N. F.; Patil, S.; Dietz, C.; Magerle, R. Identification of Nanoscale Dissipation Processes by Dynamic Atomic Force Microscopy. *Phys. Rev. Lett.* **2006**, *97*, No. 016103.
(59) Lai, C.-Y.; Cozzolino, M.; Diamanti, M. V.; Al Hassan, S.; Chiesa, M. Underlying Mechanism of Time Dependent Surface Properties of Calcite (CaCO3): A Baseline for Investigations of Reservoirs Wettability. *J. Phys. Chem. C* **2015**, *119* (52), 29038−29043.
(60) Al Mahri, M. A.; Alshehhi, M.; Olukan, T.; Vargas, M. R.; Molini, A.; Alhassan, S.; Chiesa, M. Surface alteration of calcite:

https://doi.org/10.1021/acs.jpcc.4c06040
J. Phys. Chem. C 2024, 128, 21154−21163

interpreting macroscopic observations by means of AFM. *Phys. Chem. Chem. Phys.* **2017**, *19* (37), 25634−25642.
(61) Wani, O. B.; Lai, C.-Y.; Quadri, S. M. R.; Chiesa, M.; Alhassan, S. M. Understanding the Wettability of Calcite (CaCO3) Using Higher Spatial Resolution. *Energy Fuels* **2018**, *32* (10), 10344−10353.
(62) Bruno, M.; Massaro, F. R.; Prencipe, M. Theoretical structure and surface energy of the reconstructed {01.2} form of calcite (CaCO3) crystal. *Surf. Sci.* **2008**, *602* (16), 2774−2782.
(63) Kendall, T. A.; Martin, S. T. Water-induced reconstruction that affects mobile ions on the surface of calcite. *journal of physical chemistry. A* **2007**, *111* (3), 505−14.
(64) Hansma, H. G. Surface biology of dna by atomic force microscopy. *Annu. Rev. Phys. Chem.* **2001**, *52* (Volume 52, 2001), 71−92.
(65) Rotondi, S. M. C.; Canepa, P.; Angeli, E.; Canepa, M.; Cavalleri, O. DNA Sensing Platforms: Novel Insights into Molecular Grafting Using Low Perturbative AFM Imaging. *Sensors* **2023**, *23* (9), 4557.
(66) Dai, X.; Li, Q.; Aldalbahi, A.; Wang, L.; Fan, C.; Liu, X. DNA-Based Fabrication for Nanoelectronics. *Nano Lett.* **2020**, *20* (8), 5604−5615.
(67) Main, K. H. S.; Provan, J. I.; Haynes, P. J.; Wells, G.; Hartley, J. A.; Pyne, A. L. B. Atomic force microscopy—A tool for structural and translational DNA research. *APL Bioeng.* **2021**, *5* (3), No. 031504.
(68) Voet, D.; Judith G, V. *Biochemistry*; Wiley: 1995.
(69) Zitzler, L.; Herminghaus, S.; Mugele, F. Capillary forces in tapping mode atomic force microscopy. *Phys. Rev. B* **2002**, *66* (15), No. 155436.
(70) Santos, S.; Guang, L.; Souier, T.; Gadelrab, K. R.; Chiesa, M.; Thomson, N. H. A method to provide rapid in situ determination of tip radius in dynamic atomic force microscopy. *Rev. Sci. Instrum.* **2012**, *83*, 043707−043717.
(71) Santos, S.; Barcons, V.; Christenson, H. K.; Font, J.; Thomson, N. H. The intrinsic resolution limit in the atomic force microscope: implications for heights of nano-scale features. *PLoS One* **2011**, *6* (8), No. e23821.
(72) Tamayo, J.; Garcia, R. Relationship between phase shift and energy dissipation in tapping-mode scanning force microscopy. *Appl. Phys. Lett.* **1998**, *73* (20), 2926−2928.
(73) Anczykowski, B.; Gotsmann, B.; Fuchs, H.; Cleveland, J. P.; Elings, V. B. How to measure energy dissipation in dynamic mode atomic force microscopy. *Appl. Surf. Sci.* **1999**, *140* (3), 376−382.
(74) Lozano, J. R.; Garcia, R. Theory of phase spectroscopy in bimodal atomic force microscopy. *Phys. Rev. B* **2009**, *79* (1), No. 014110.
(75) Leckband, D.; Israelachvili, J. Intermolecular forces in biology. *Q. Rev. Biophys.* **2001**, *34* (2), 105−267.
(76) Hamaker, H. C. The London − van der Waals attraction between spherical particles. *Physica* **1937**, *4* (10), 1058−1072.
(77) Santos, S. Phase contrast and operation regimes in multi-frequency atomic force microscopy. *Appl. Phys. Lett.* **2014**, *104* (14), No. 143109.
(78) Santos, S.; Gadelrab, K.; Lai, C.-Y.; Olukan, T.; Font, J.; Barcons, V.; Verdaguer, A.; Chiesa, M. Advances in dynamic AFM: From nanoscale energy dissipation to material properties in the nanoscale. *J. Appl. Phys.* **2021**, *129* (13), No. 134302.
(79) Santos, S.; Gadelrab, K. R.; Silvernail, A.; Armstrong, P.; Stefancich, M.; Chiesa, M. Energy dissipation distributions and dissipative atomic processes in amplitude modulation atomic force microscopy. *Nanotechnology* **2012**, *23* (12), No. 125401.

https://doi.org/10.1021/acs.jpcc.4c06040
J. Phys. Chem. C 2024, 128, 21154−21163